

Modeling of self-excited forces during multimode flutter: an experimental study

Bartosz Siedziako* and Ole Øiseth^a

Department of Structural Engineering, Norwegian University of Science and Technology,
Richard Birkelands vei 1A, 7491 Trondheim, Norway

(Received November 11, 2017, Revised May 31, 2018, Accepted June 1, 2018)

Abstract. The prediction of multimode flutter relies, to a larger extent than bimodal flutter, on accurate modeling of the self-excited forces since it is challenging to perform experimental validation by using aeroelastic tests for a multimode case. This paper sheds some light on the accuracy of predicted self-excited forces by comparing numerical predictions of self-excited forces with measured forces from wind tunnel tests considering the flutter vibration mode. The critical velocity and the corresponding flutter vibration mode of the Hardanger Bridge are first determined using the classical multimode approach. Then, a section model of the bridge is forced to undergo a motion corresponding to the flutter vibration mode at selected points along the bridge, during which the forces that act upon it are measured. The measured self-excited forces are compared with numerical predictions to assess the uncertainty involved in the modeling. The self-excited lift and pitching moment are captured in an excellent manner by the aerodynamic derivatives. The self-excited drag force is, on the other hand, not well represented since second-order effects dominate. However, the self-excited drag force is very small for the cross-section considered, making its influence on the critical velocity marginal. The self-excited drag force can, however, be of higher importance for other cross-sections.

Keywords: forced vibration test; flutter; bridge aerodynamics; section model; aerodynamic derivatives

1. Introduction

Wind-induced vibrations are of particular importance when designing long-span bridges. Bridge design needs to prevent vibrations due to vortex shedding at low mean wind velocity and due to turbulence in a wind field under strong winds. Furthermore, the aeroelastic stability limit of the combined structure and flow system needs to be sufficiently high to prevent collapse due to static divergence, galloping and flutter. In particular, flutter has received much attention among researchers and bridge engineers since the Tacoma Narrows Bridge collapsed due to flutter in 1940. However, since technological progress makes it possible to build longer and more slender bridges, the flutter of suspension and cable-stayed bridges remains an active research field. Flutter is in fact one of the most important research topics related to Coastal Highway Route E39 (Dunham 2016), regarding which the Norwegian Public Roads Administration is investigating the possibility to replace several ferries with suspension bridges that have spans up to 3700 meters.

Motion-induced or so-called self-excited forces cause flutter instability. These forces can be modeled in many ways, but the model involving aerodynamic derivatives developed by Scanlan and co-workers (Scanlan and Tomko 1971) is the most common approach when assessing the flutter stability limit of bridges. The aerodynamic

derivatives are assumed as functions only of reduced velocity and can be identified via wind tunnel tests or computational fluid dynamics (CFD) simulations (Huang *et al.* 2009, Sarwar *et al.* 2008, Zhu *et al.* 2007). One of the major challenges in using CFD is to accurately model the flow in the boundary layer around railings and other bridge deck details since this might have a significant impact on the accuracy of the outcome of the simulations (Jones *et al.* 1995, Sarwar *et al.* 2008, Takizawa *et al.* 2014). Wind tunnel tests therefore remain of crucial importance in bridge design.

The flutter speed is assessed using various methods, from simple formulas to advanced finite element methodologies. More than 50 years ago, Selberg (1961) derived a formula for the critical velocity that is very accurate if the aerodynamic properties of the bridge deck are similar to those of an ideal flat plate and if the still-air vertical and torsional vibration modes are shape-wise similar. The formula is still currently used in preliminary designs worldwide despite the fact that more sophisticated formulas, which allow taking into account structural damping, some of the aerodynamic derivatives and shape-wise similarity, have been developed more recently (Bartoli and Mannini 2008, Chen 2007, Nakamura 1978, Øiseth and Sigbjørnsson 2011). It is also possible to evaluate the flutter stability limit by directly observing a scaled section model of a bridge in a wind tunnel (e.g., Andersen *et al.* 2016, Costa 2007, Gu *et al.* 2000, Iwamoto and Fujino 1995, Körlin and Starossek 2007, Manzoor *et al.* 2011). However, it is sometimes difficult to very accurately define regions where the section model is stable/unstable. In addition, the method itself implies that it is hard to consider more than two vibration modes. The simplified methods are

*Corresponding author, Ph.D. candidate

E-mail: bartosz.siedziako@ntnu.no

^a Ph.D.

E-mail: ole.oiseth@ntnu.no

insufficient for long-span bridges. More precise results can be provided by using effective numerical methods such as complex eigenvalue analysis (Simiu and Scanlan 1996) or the step-by-step method (Matsumoto *et al.* 2007, 2008), using aerodynamic derivatives as the input. Several authors have emphasized the importance of aerodynamic derivatives related to lateral motion when assessing the flutter stability limit (Sarkar *et al.* 2004, Singh *et al.* 1996, Zhang and Brownjohn 2005) as well as the significance of contributions from secondary still-air vibration modes (Katsuchi *et al.* 1998, Ø iseth *et al.* 2010) in the flutter mode. Previous studies have, for example, showed that six primary still-air modes play a significant role in the flutter mechanism of the Akashi-Kaikyo Bridge (Katsuchi *et al.* 1999, Miyata *et al.* 1994), which is currently the world's longest suspension bridge. Thus, current state-of-the-art flutter assessment involves horizontal motion, which can readily be included in the multimode approach (e.g., Katsuchi *et al.* 1998, Salvatori and Borri 2007) or in the more direct finite element approach (Ge and Tanaka 2000, Hua and Chen 2008, Mishra *et al.* 2008, Namini *et al.* 1992, Ø iseth *et al.* 2012). Alternatively, the flutter stability limit can be assessed by studying the free vibration response of a system in the time domain, which requires modeling of the self-excited forces by using either indicial (Caracoglia and Jones 2003) or rational functions (Xu *et al.* 2017).

Reliable and accurate experimental data of all 18 aerodynamic derivatives are crucial when including horizontal motion in the flutter assessment. It is also important that the load model holds for the cross-section considered. The forced vibration setup first used by Ukeguchi *et al.* (1966) and later further developed to include horizontal motion is therefore often used to identify aerodynamic derivatives, as it is considered more reliable (Diana *et al.* 2015) than free vibration tests and suitable for larger velocities, motion amplitudes and turbulence intensity (Cao and Sarkar 2012, Sarkar *et al.* 2009). The section model is forced to undergo a pure horizontal, vertical or torsional single harmonic motion while the drag and lift forces as well as the pitching moment are measured during a forced vibration test. However, as aptly noted in Zhu *et al.* (2007), forcing bridge decks in this manner does not reflect real bridge behavior in strong wind. Previous studies have also shown that the aerodynamic derivatives might depend on the amplitudes of vibration (Chen *et al.* 2005, Scanlan 1997), the torsional-vertical frequency ratio (Qin *et al.* 2009) and the number of degrees of freedom considered during tests (Matsumoto 1996). Keeping these issues in mind, the authors were concerned regarding whether the aerodynamic derivatives identified by applying the standard procedure are sufficient to predict the self-excited forces that occur during flutter or if a more advanced nonlinear methodology needs to be applied (Diana *et al.* 2008, Wu and Kareem 2014).

The flutter motion is a single frequency motion and is, in this sense, simple compared to the buffeting response. The ratios of the amplitudes of the horizontal, vertical and torsional motions are, however, different along the span, and the flutter vibration mode is furthermore complex, which makes the phase shift between the horizontal, vertical

and torsional motions vary along the span. The accuracy of the linear load model is investigated in this study by measuring the self-excited forces acting on a section model of the Hardanger Bridge when it is forced to undergo the flutter motion obtained by solving the complex eigenvalue problem of the aeroelastic system. First, the aerodynamic derivatives of a detailed section model of the bridge deck, including both railings and guide vanes, are identified using the standard forced vibration procedure. A state-of-the-art multimode flutter analysis is conducted to obtain the critical mode shape. The flutter motion is then applied at several locations along the span while measuring the self-excited forces in wind tunnel tests using a recently developed forced vibration setup (Siedziako *et al.* 2017a). The results are compared with predictions by applying the aerodynamic derivatives obtained from the standard forced vibration tests. Possible amplitude dependency, as, for instance, reported by Chen *et al.* (2005), is investigated by measuring the self-excited forces when the amplitudes of vibration are exponentially increasing. This simulates divergent behavior corresponding to negative damping of an aeroelastic system.

2. Flutter analysis of the Hardanger Bridge

2.1 Critical velocity

In order to perform wind tunnel tests corresponding to multimode flutter it is necessary to obtain the critical velocity and the corresponding flutter vibration mode for the bridge considered. Fig. 1 shows the Hardanger Bridge, which crosses the Hardanger Fjord in Norway. It has a main span of 1310 m, which is currently the longest in Norway, and towers that are 186 m high. The bridge is very slender since it only has two lanes for traffic and one lane for pedestrians, making the distance between the two main cables only 14.5 m. Mass and mass moment of inertia equal to respectively 8825 kg/m and 222840 kgm²/m. The Hardanger Bridge has been extensively studied at NTNU (Ø iseth *et al.* 2010, 2011), and current research activities also include a large monitoring program in which wind velocities and accelerations are measured at several locations along the bridge deck and at the top of each tower (Fenerci and Ø iseth 2015, 2017, Fenerci *et al.* 2017). Flutter stability was one of the major concerns in the design of the bridge, particularly since several still-air vibration modes participate in the flutter motion.

Fig. 2 shows the finite element model representing the starting point of the flutter analysis. It is possible to introduce the self-excited forces in the finite element modeling and to assess the flutter stability limit considering all degrees of freedom (Ge and Tanaka 2000, Mishra *et al.* 2008, Namini *et al.* 1992, Ø iseth *et al.* 2012). However, a reduced-order model using selected still-air vibration modes as generalized coordinates, commonly referred to as the multimode approach (Chen *et al.* 2001, Ge and Tanaka 2000, Jain *et al.* 1996, Katsuchi *et al.* 1998, 1999, Matsumoto *et al.* 2008, Salvatori and Borri 2007, Scanlan *et al.* 1990), is used in this paper. Having the generalized properties of all the selected vibration modes, the self-excited forces need to



Fig. 1 The Hardanger Bridge (photograph by Ole Ø iseth)

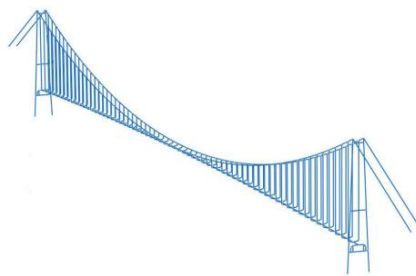


Fig. 2 An ABAQUS FE model of the Hardanger Bridge

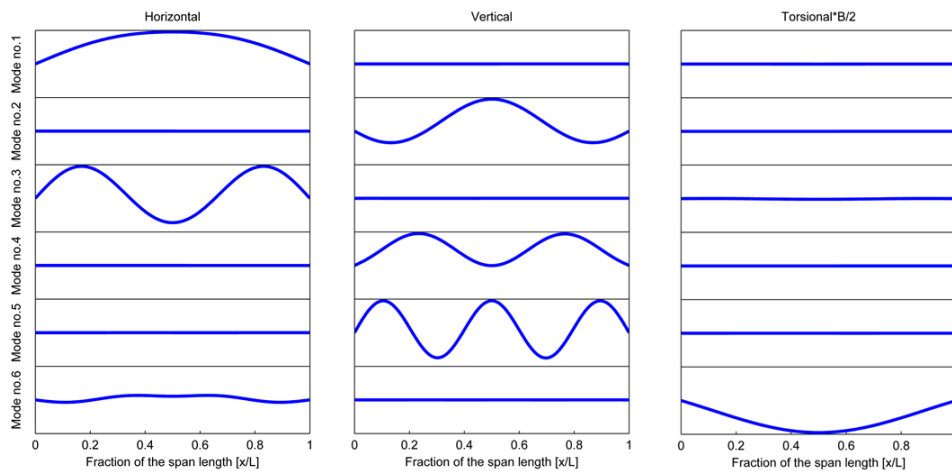


Fig. 3 Still-air vibration modes of the Hardanger Bridge used in the flutter analysis. The amplitude vibrations of each mode were scaled such that maximum displacement is equal to unity

be included in the modeling. Only self-excited forces acting on the girder are considered when obtaining the critical velocity and the corresponding flutter mode since self-excited forces acting on cables and towers are considered to be of minor importance. The response along the girder is given by

$$\mathbf{u}(x,t) = \mathbf{\Psi}(x)\boldsymbol{\eta}(t) \quad (1)$$

$$\mathbf{\Psi}(x) = [\boldsymbol{\varphi}_1, \boldsymbol{\varphi}_2, \dots, \boldsymbol{\varphi}_N], \quad \boldsymbol{\varphi}_i = [\varphi_{i,v}, \varphi_{i,z}, \varphi_{i,\theta}]^T, \quad \boldsymbol{\eta}(t) = [\eta_1, \eta_2, \dots, \eta_N]^T$$

Here, $\mathbf{\Psi}$ represents the selected still-air vibration modes and $\boldsymbol{\eta}$ the corresponding generalized coordinates. Fig. 3

shows the still-air vibration modes considered in the flutter analysis, while Table 1 presents the generalized properties. The generalized masses for each mode have been extracted from an ABAQUS model and were calculated based on the default eigenvector normalization, which was scaled so that the largest entry in each vector is unity.

The flutter stability limit can be assessed by considering the characteristic equation of the combined structure and flow system (Agar 1989, Kvåle *et al.* 2016).

Table 1 Natural frequencies, damping ratios and modal masses of the selected still-air vibration modes of the Hardanger Bridge

Mode no.	Period T [s]	Frequency		Damping ξ [%]	Modal mass \tilde{M}_0 [kg]/[kgm ²]	Type
		ω [rad/s]	f [Hz]			
1	19.98	0.316	0.050	0.5	$8.56 \cdot 10^7$	Hor.
2	7.11	0.884	0.141	0.5	$4.44 \cdot 10^7$	Ver.
3	5.91	1.062	0.169	0.5	$5.71 \cdot 10^7$	Hor.
4	5.07	1.239	0.197	0.5	$6.68 \cdot 10^7$	Ver.
5	3.67	1.712	0.273	0.5	$7.27 \cdot 10^7$	Ver.
6	2.78	2.260	0.360	0.5	$5.63 \cdot 10^7$	Tor.

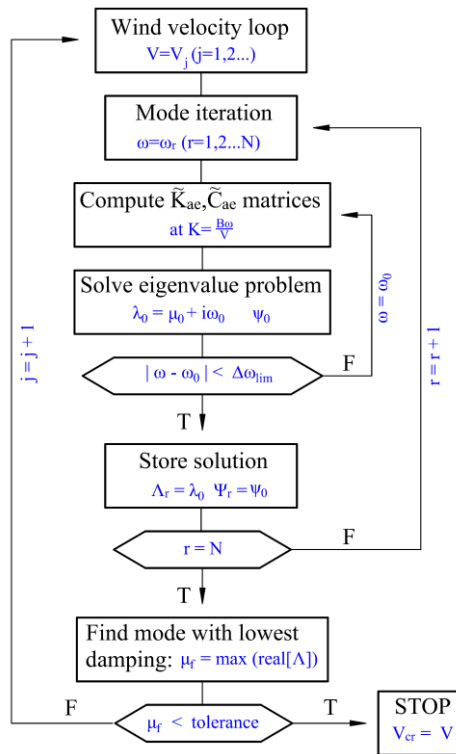


Fig. 4 Algorithm used to calculate the critical velocity and the corresponding flutter vibration mode

$$\left(\lambda^2 \bar{\mathbf{M}}_0 + \lambda (\bar{\mathbf{C}}_0 - \bar{\mathbf{C}}_{ae}(V, \omega)) + (\bar{\mathbf{K}}_0 - \bar{\mathbf{K}}_{ae}(V, \omega)) \right) \boldsymbol{\phi} = \mathbf{0} \quad (2)$$

Here, λ is the eigenvalue, $\boldsymbol{\phi}$ is the corresponding eigenvector, and $\bar{\mathbf{M}}_0$, $\bar{\mathbf{C}}_0$ and $\bar{\mathbf{K}}_0$ represent the still-air generalized mass damping and stiffness matrices. The generalized aerodynamic damping and stiffness matrices are obtained by considering the self-excited forces acting on the girder as follows

$$\begin{aligned} \bar{\mathbf{K}}_{ae}(V, \omega) &= \int_L \boldsymbol{\Psi}^T(x) \mathbf{K}_{ae}(V, \omega) \boldsymbol{\Psi}(x) dx \\ \bar{\mathbf{C}}_{ae}(V, \omega) &= \int_L \boldsymbol{\Psi}^T(x) \mathbf{C}_{ae}(V, \omega) \boldsymbol{\Psi}(x) dx \end{aligned} \quad (3)$$

The aerodynamic non-symmetric stiffness, \mathbf{K}_{ae} , and damping, \mathbf{C}_{ae} , matrices are most commonly represented by experimentally determined aerodynamic derivatives, as proposed by Scanlan and Tomko (Scanlan and Tomko 1971).

$$\mathbf{C}_{ae} = \frac{1}{2} \rho V K B \begin{bmatrix} P_1^* & P_5^* & B P_2^* \\ H_5^* & H_1^* & B H_2^* \\ B A_5^* & B A_1^* & B^2 A_2^* \end{bmatrix} \quad \mathbf{K}_{ae} = \frac{1}{2} \rho V^2 K^2 \begin{bmatrix} P_4^* & P_6^* & B P_3^* \\ H_6^* & H_4^* & B H_3^* \\ B A_6^* & B A_4^* & B^2 A_3^* \end{bmatrix} \quad (4)$$

Here, V is the mean wind velocity; ρ is the air density; B is the width of the cross-section; $K = B\omega/V$ is the reduced frequency of motion. P_n^* , H_n^* , and A_n^* , $n \in \{1, 2, \dots, 6\}$, are the dimensionless aerodynamic derivatives, which are functions of the reduced frequency and are most commonly considered as cross-sectional properties. The eigenvalues need to be solved in an iterative manner since the elements in the aerodynamic stiffness and damping matrices are functions of the reduced frequency of motion and thus the

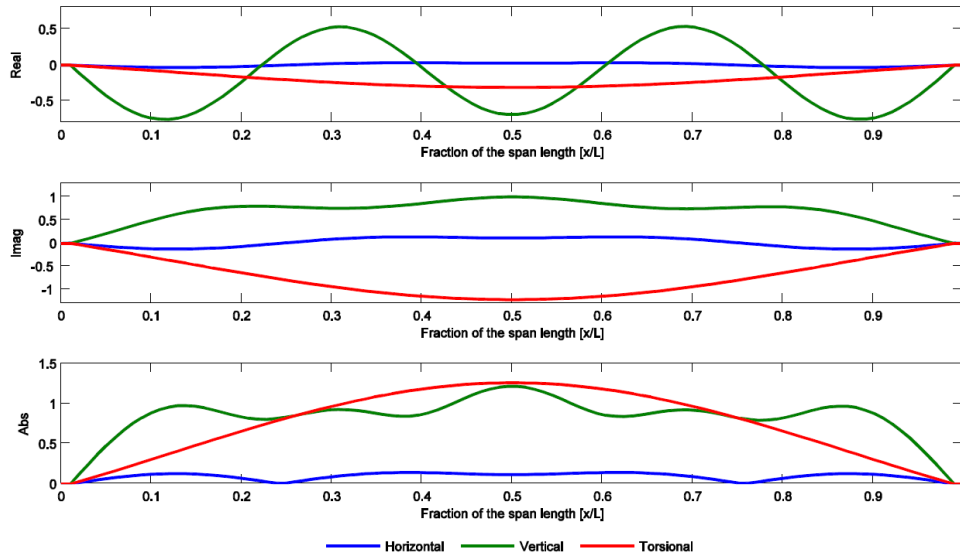


Fig. 5 Motion along the girder corresponding to the flutter mode of the Hardanger Bridge. The top figure corresponds to the real part, the middle figure corresponds to the imaginary part and the bottom figure corresponds to the absolute value

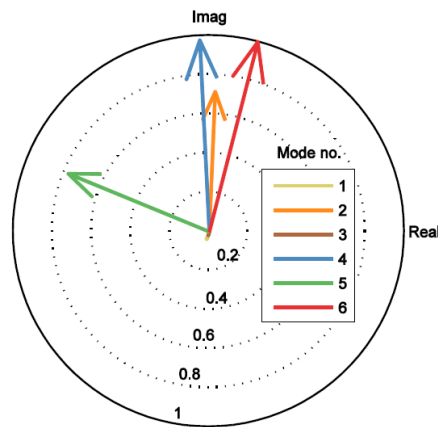


Fig. 6 Argand diagram showing contributions from each of the still-air modes in the flutter mode. The eigenvector ϕ_{CR} was normalized to make its maximum absolute value equal to 1

imaginary part of the eigenvalues. Fig. 4 illustrates the algorithm used in this study built in by authors in matlab function, which has been used for example by Ø iseth *et al.* (2010, 2011).

The free vibration response (in generalized coordinates) can be expressed as

$$\eta(t) = \sum_{r=1}^{2N} A_r \phi_r e^{\lambda_r t} \quad (5)$$

Here, the values of the constant A_r are obtained by considering the initial conditions of the problem. The solution of the eigenvalue problem renders $2N$ eigenvalues and eigenvectors that come in complex conjugate pairs $\lambda_r = \mu_r \pm i\omega_r$, making the total response in Eq. (5) real. The stability limit is defined as the lowest wind speed at which the real part of one of the eigenvalues becomes positive, which corresponds to negative damping that results in a divergent response.

$$\xi = -\frac{\text{Re}[\lambda_r]}{|\lambda_r|} \approx 0 \rightarrow \mu_i \approx 0 \quad (6)$$

Since the flutter problem is solved iteratively, the real part of the critical eigenvalue, μ_{CR} , is not exactly zero but rather approaches this value at higher wind velocities. In this study, the flutter is recognized when μ_{CR} drops below a tolerance level set at 0.001. For the frequency iterations, a limit of $\Delta\omega_{lim} = 0.0001$ is set as the convergence criterion, usually achieved in the third iteration.

The aerodynamic derivatives obtained during the design of the bridge presented by Svend Ole Hansen ApS (2009) are used in the flutter analysis. All the still-air vibration modes considered are assigned a damping of 0.5% and rotations of the bridge decks about its longitudinal axis due the mean value of the wind load is neglected and thereby static deformations as well. The obtained critical velocity and frequency for the Hardanger Bridge are respectively

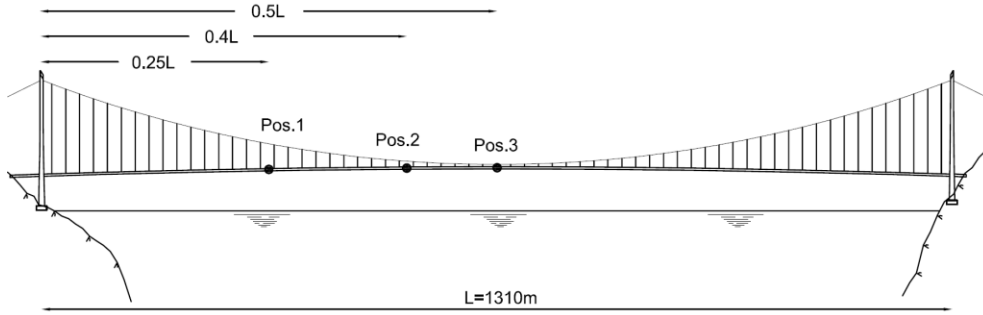


Fig. 7 Selected locations at which the self-excited forces are assessed by comparing numerical simulations and wind tunnel tests

Table 2 Combinations of mean wind velocity and frequency of motion considered in the comparative study

No.	Frequency scale S_f	Geometry scale S_g	Wind tunnel air velocity [m/s]	Frequency of motion in the wind tunnel		Critical frequency [Hz]	Reduced velocity [-]
				ω [rad/s]	f [Hz]		
1	4	1/50	6.59	7.012	1.116	0.279	2.57
2	6	1/50	9.89	10.52	1.674	0.279	2.57
3	7	1/50	11.53	12.27	1.953	0.279	2.57

82.38 m/s and 0.279 Hz giving reduced velocity, at which flutter occurs equals 2.57. Fig. 5 shows the corresponding flutter mode in terms of the real and the imaginary part of the displacements along the girder. The figure illustrates that the flutter motion is three dimensional, with dominating vertical and torsional components, and that there are significant phase shifts between the considered response components. The modal complexity of the flutter motion is also illustrated using an Argand diagram of the vector ϕ_{CR} (eigenvector corresponding to the eigenvalue with zero real part) displayed in Fig. 6, which also shows the participation of the still-air modes in the flutter mode.

2.2 Flutter motion for wind tunnel testing

The flutter motion will vary along the girder since the still-air modes have varying amplitudes along the span of the bridge, which also makes the phase shifts between the horizontal, vertical and torsional motions change. It is not possible to consider many points along the girder, but looking at Fig. 5 the points shown in Fig. 7, seems representative both with respect to amplitude and phase angle between vertical and torsional motion and are therefore considered in this study.

The flutter motion history at the selected points can be obtained by solving

$$\mathbf{u}_n(t) = A_{CR} \mathbf{\Phi}(x_n) \text{Re}[\phi_{CR} e^{\omega_{CR} t (-\xi + i)}] \quad (7)$$

Here, the constant A_{CR} is determined by considering the initial conditions. The tests need to be performed at with the same reduced velocity at the model scale as at full scale according to the following relation.

$$\frac{V_{MS}}{B_{MS} \omega_{MS}} = \frac{V_{FS}}{B_{FS} \omega_{FS}} \quad (8)$$

Here, V is the mean wind velocity, B is the width of the girder and ω is the frequency of motion. The subindexes FS and MS denote full scale and model scale, respectively. The mean wind velocity at the model scale is then given by

$$V_{MS} = \frac{B_{MS}}{B_{FS}} \frac{\omega_{MS}}{\omega_{FS}} V_{FS} = S_g S_f V_{FS} \quad (9)$$

Here, S_g and S_f represent the geometry and frequency scale factors. The section model of the Hardanger Bridge has a scale of 1:50, and the considered mean wind velocity and frequency of motion can be varied in the wind tunnel tests. Table 2 summarizes the three different combinations of mean wind velocities and frequencies considered.

The scaled flutter motion at the selected locations at the model scale is defined by

$$\mathbf{u}_n = A_{CR} \mathbf{S}_G \mathbf{\Phi}(x_n) \text{Re}[\phi_{CR} e^{\omega_{CR} S_f t (-\xi + i)}] \quad (10)$$

Here, the matrix \mathbf{S}_G scales the horizontal, vertical and torsional displacements and is thus defined as follows.

$$\mathbf{S}_G = \begin{bmatrix} S_g & 0 & 0 \\ 0 & S_g & 0 \\ 0 & 0 & 1 \end{bmatrix} \quad (11)$$

The eigenvector ϕ_{CR} is normalized to make its maximum absolute value equal to 1 before generating the flutter motion. The constant A_{CR} is taken as one, while the damping ratio ξ is simply taken as zero. This yields a 7.89° rotation and a 1.22 m vertical displacement at the mid-span of the Hardanger Bridge and corresponds to 7.89° and 24.3 mm at the model scale. These values are larger than the typical amplitudes used in forced vibration tests but still much lower than the motion observed during the collapse of the Tacoma Narrow Bridge, where rotations of up to 35° were observed (Fuller *et al.* 2000). Fig. 8 shows Argand

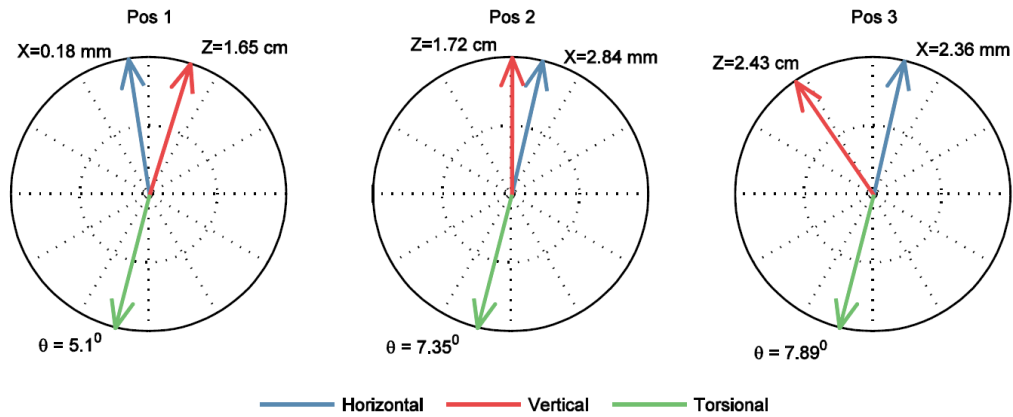


Fig. 8 Argand diagrams showing the complexity of the flutter motion at the considered locations. The lengths of the vectors are scaled to make the phase shifts between the components clearer

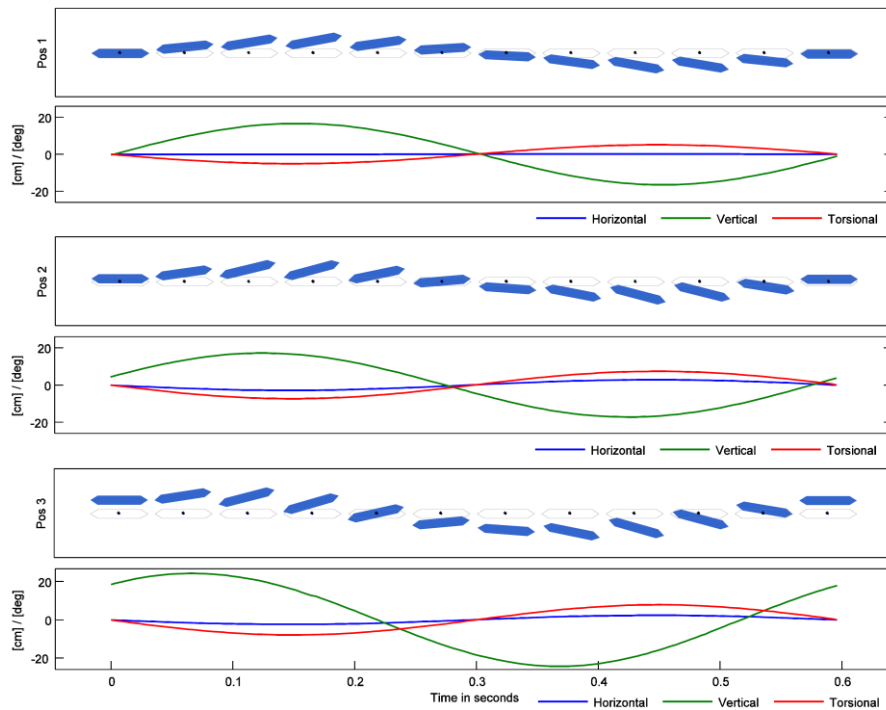


Fig. 9 Time histories of the motion of the bridge deck at three different locations during flutter motion. The coordinate system and wind direction are according to Fig. 4

diagrams of the horizontal, vertical and torsional responses at the three considered locations. At position 1, the torsional and vertical motions are close to 180 degrees out of phase, making the maximum values occur simultaneously but with opposite signs. The angle between the vertical and torsional responses is approximately 170 degrees at position 2, which will cause a time lag between the maximum vertical and torsional response, while this is even higher for point 3. Fig. 9 shows the response histories together with a visualization of the motion of the girder. It is observed that the flutter motion is different at the three positions considered in terms of the magnitude of the components and the time lags between the components.

3. Wind tunnel tests of the flutter motion

3.1 Wind tunnel and forced vibration rig

The wind tunnel tests are carried out in the Fluid Mechanics Laboratory at NTNU. The wind tunnel used in this study is a low-speed, closed-loop wind tunnel with an 11 m-long, 2 m-high and 2.7 m-wide test section. A pitot probe placed 6.10 m in front of the section model is used to measure the air velocity during the experiments. The velocity profile at the inlet of the wind tunnel is uniform, with a turbulence intensity of 0.2% (Adaramola and Krogstad 2009). A recently developed forced vibration rig

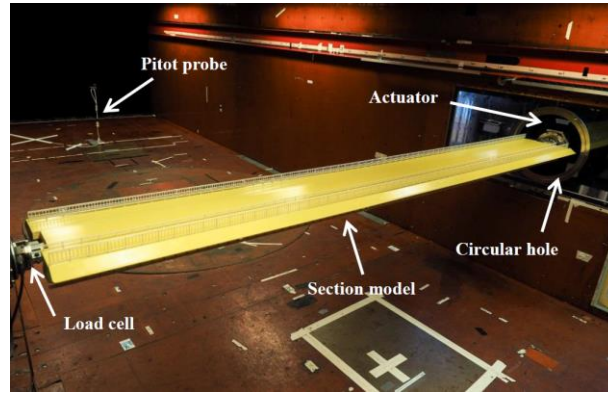


Fig. 10 Photograph showing the section model used during testing

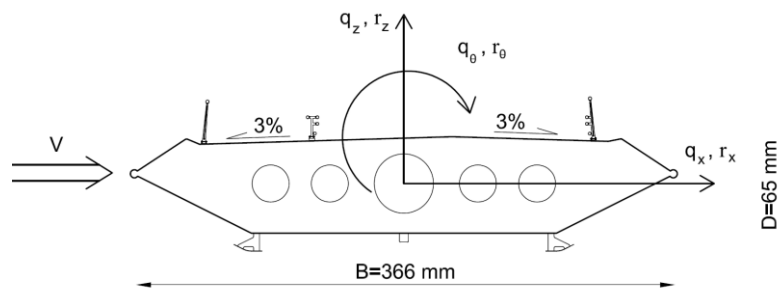


Fig. 11 The cross-section of the Hardanger Bridge deck

was used in the experiments. It is able to force arbitrary motion histories in the heaving, swaying and torsional directions simultaneously. For further details on the setup components, motion control and data acquisition see (Siedziako *et al.* 2017). The data acquisition was slightly modified in this study to utilize the advantages of the CompactRIO platform (NI CompactRIO 2017) over CompactDAQ and currently NI cRIO-9067 equipped with NI 9239 analog input modules is adopted to acquire the voltage signals from the controller, the load cells and the pressure transducer that is connected to the pitot probe. Therefore a comprehensive LabVIEW program is used to communicate with the actuators controller to upload the motion histories, while a separate LabVIEW program based on the CompactRIO platform is used to acquire data. The sampling rate for the data acquisition is set to 2 kHz, downsampled to 250 Hz, and a time step of 1 ms is used for the uploaded motion histories.

3.2 Section model

Fig. 10 shows a Hardanger Bridge section model used in this study mounted between two actuators. It is 2.68 m long, and there are only 1.5 cm gaps between the ends of the model and the wind tunnel walls, making end plates unnecessary. The dimensions of the cross-section are presented in Fig. 11. The section model consists of an aluminum pipe, with an outer diameter of 40 mm and a wall thickness of 1 mm that provides most of the stiffness of the model. The aluminum pipe is clamped firmly to the

actuators on both sides of the wind tunnel. The geometry of the bridge deck is milled in Gurit PVC 60, which is glued onto the aluminum pipe, while the bridge railings and guide vanes are 3D printed. The mass of the section model is 5.45 kg (2.03 kg/m), and its first natural frequency is 12.5 Hz. More details about the experimental setup and the section model are given in (Siedziako *et al.* 2017)

3.3 Aerodynamic derivatives

The flutter stability limit and the corresponding flutter mode were obtained using data from the free vibration tests conducted at Svend Ole Hansen ApS (2009), while all the tests presented in this paper were conducted in the Fluid Mechanics laboratory at NTNU during the same period. It is well known that the aerodynamic derivatives from different wind tunnels that use different methods to process the data might yield slightly different aerodynamic derivatives; see, for instance, (Sarkar *et al.* 2009), where this phenomenon has been studied in detail. This makes it necessary to determine the aerodynamic derivatives for the actual test conditions. The self-excited forces acting on a bridge deck can, according to the load model proposed by Scanlan and coworkers, be expressed as (Scanlan and Tomko 1971)

$$\mathbf{q}_{se}(K, t) = \mathbf{C}_{ae}(K) \dot{\mathbf{u}}(t) + \mathbf{K}_{ae}(K) \mathbf{u}(t) \quad (12)$$

The matrices and symbols involved were introduced in Eq. (4), and Fig. 11 shows the positive directions of the motion and forces. The identification method used herein is a time domain method based on the work of Han *et al.*

Table 3 Summary of the properties, frequencies and amplitudes used in the standard forced vibration tests

Duration of time series	50 s	Tested velocities	4, 6, 8, and 10 m/s
Total number of tests	84	Tested frequencies	0.5, 0.8, 1.1, 1.4, 1.7, 2.0, 2.5 Hz
Tested reduced velocities	28	Reduced velocity range	From 0.7 to 8.7
Sampling frequency	250 Hz	Vibration amplitudes	1.5 cm / 2°

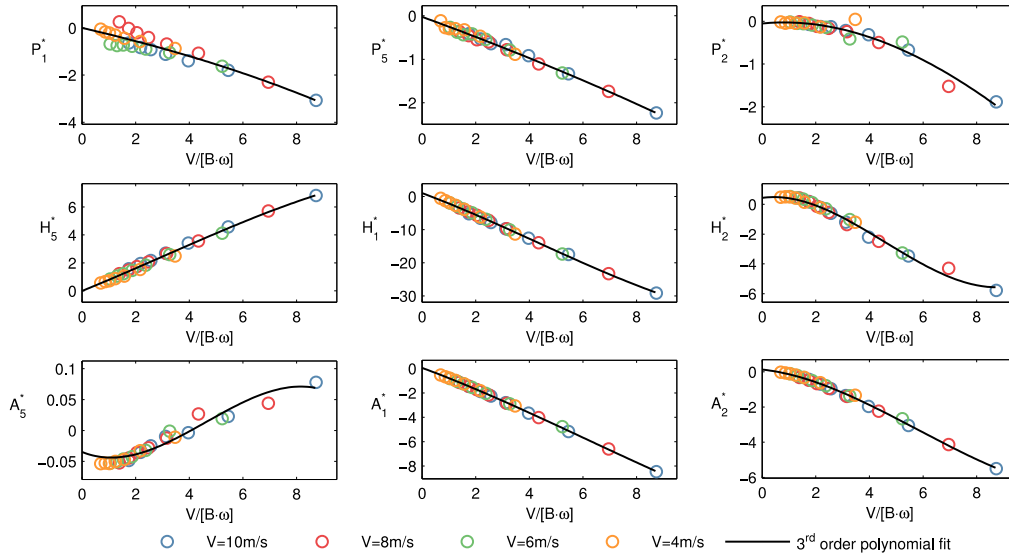


Fig. 12 Aerodynamic derivatives of the Hardanger Bridge related to velocities or angular velocities

(2014), where the model of aeroelastic forces is fitted to the time series of the self-excited forces by a least squares fit. An extended version of this method that can address more complicated motion patterns was recently developed in (Siedziako *et al.* 2016b). It was decided to consider horizontal, vertical and torsional motion separately in this paper since this makes the identified aerodynamic derivatives more reliable. It is however possible to combine all three motions if one ensures that all motions give significant contributions to the measured self-excited forces although the identification might become more difficult. By considering only the sinusoidal pitching motion, the self-excited forces given in Eq. (12) can be written in a matrix form.

$$\mathbf{q}_{se,\theta}(t, K, V) = \mathbf{X}_\theta \mathbf{E}_\theta \quad (13)$$

Here, $\mathbf{q}_{se,\theta}(t, K, V)$ represents the self-excited forces induced by the torsional motion, the coefficient matrix \mathbf{E}_θ contains the aerodynamic derivatives, and the matrix \mathbf{X}_θ contains the torsional motion history.

$$\mathbf{E}_\theta = \frac{1}{2} \rho V^2 B \begin{bmatrix} B K P_2^* / V & B K H_2^* / V & B^2 K A_2^* / V \\ K^2 P_3^* & K^2 H_3^* & B K^2 A_3^* \end{bmatrix} \quad (14)$$

$$\mathbf{X}_\theta = \begin{bmatrix} \bullet & \\ r_{\theta,1} & r_{\theta,1} \\ \bullet & \\ r_{\theta,2} & r_{\theta,2} \\ \vdots & \vdots \\ r_{\theta,n} & r_{\theta,n} \end{bmatrix} \quad \mathbf{q}_{se} = \begin{bmatrix} q_{se,x,1} & q_{se,z,1} & q_{se,\theta,1} \\ \vdots & \vdots & \vdots \\ q_{se,x,n} & q_{se,z,n} & q_{se,\theta,n} \end{bmatrix} \quad (15)$$

The coefficient matrix \mathbf{E}_θ and thus the 6 aerodynamic derivatives related to the torsional motion can then be obtained by minimizing the sum of squares.

$$\mathbf{E}_\theta = (\mathbf{X}_\theta^T \mathbf{X}_\theta)^{-1} \mathbf{X}_\theta^T \mathbf{q}_{se} \quad (16)$$

Similar expressions for \mathbf{E}_z and \mathbf{E}_x are analogously derived by considering the vertical and horizontal motion, respectively. In the tests presented here, the time histories of the aeroelastic forces have been extracted by repeating each test under still-air conditions. Then, the forces recorded in still air can be directly subtracted from the time series recorded in wind to remove the inertia forces; see also (Diana *et al.* 2004) and (Siedziako *et al.* 2016a). Buffeting forces due to turbulence can be neglected since the tests were conducted in smooth flow. Any static contributions from both the mean wind and gravity are removed by detrending the measured forces.

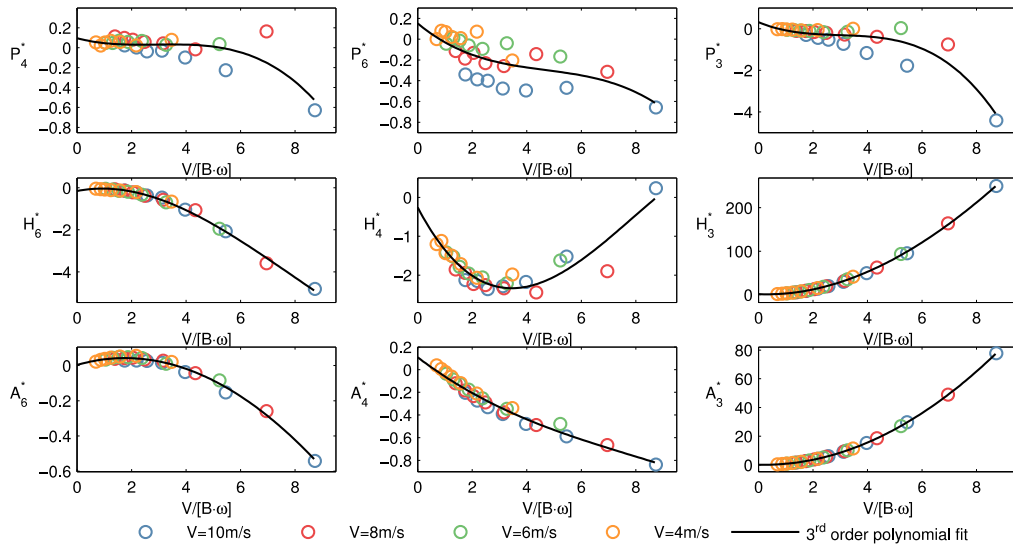


Fig. 13 Aerodynamic derivatives of the Hardanger Bridge related to displacements or rotation

Table 4 Aerodynamic derivatives at $V_{red} = 2.57$ calculated using the third-order polynomial fit to the data

AD	P_1^*	P_2^*	P_3^*	P_4^*	P_5^*	P_6^*
Value	-0.733	-0.135	-0.286	0.031	-0.622	-0.197
AD	H_1^*	H_2^*	H_3^*	H_4^*	H_5^*	H_6^*
Value	-7.52	-0.510	20.66	-2.22	2.09	-0.357
AD	A_1^*	A_2^*	A_3^*	A_4^*	A_5^*	A_6^*
Value	-2.23	-0.911	6.10	-0.280	-0.032	0.035

The aerodynamic derivatives were determined considering the mean wind velocity and frequency combinations shown in Table 3. The aerodynamic derivatives for the Hardanger Bridge cross-section, including both guide vanes and railings, are presented in Fig. 12 and Fig. 13 together with a third-order polynomial fit to the data. Nearly the exact same mode shape of the flutter mode was obtained when using the aerodynamic derivatives provided by Svend Ole Hansen ApS (2009) as identified in this study; therefore, there was no need to repeat the flutter tests.

3.4 Flutter motion

The time series of the flutter motion at the wind tunnel scale was obtained using Eq. (10). Time series of 120, 60 and 68 s duration for the 4, 6, and 7 frequency scales corresponding to 1.12, 1.67 and 1.95 Hz at the model scale, respectively, were used in the tests to obtain a reasonable number of cycles. Each time series was tested at only one wind speed, as depicted in Table 2, since the reduced velocities at the model and full scales need to be in agreement. The values of the aerodynamic derivatives at the critical reduced velocity $\hat{V}_{CR} = 2.57$ are displayed in the Table 4. The presented values were calculated using the third-order polynomial fit to the aerodynamic derivatives.

The correlation coefficient of the predicted and measured time series of the self-excited forces is used to evaluate the performance of the load model.

$$\rho_{xy} = \frac{\sum_{i=1}^n x_i y_i}{\sigma_x \sigma_y n} \quad (17)$$

A measure of the accuracy of the predicted peak values is also used to evaluate the results.

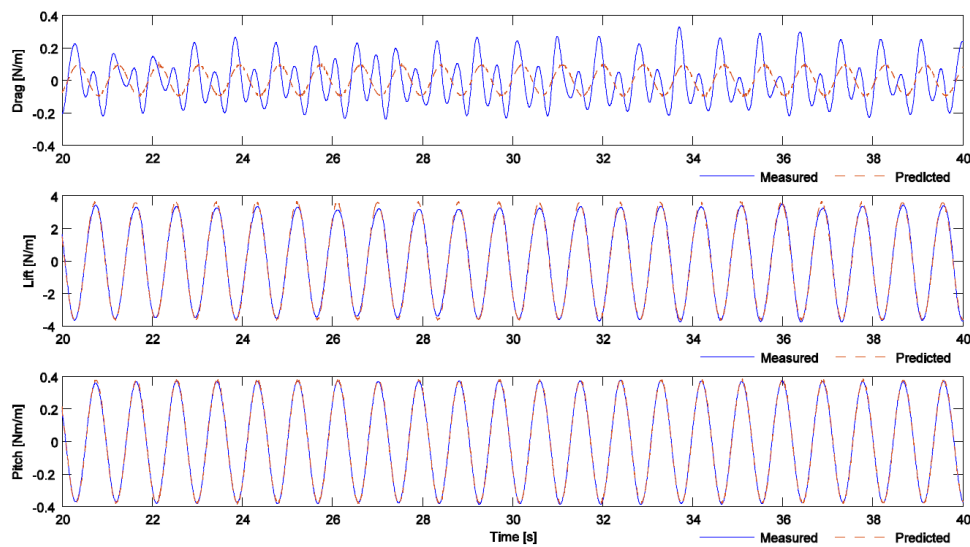
$$P_{err} = \frac{\sum_{i=1}^n (\bar{x}_i - \bar{y}_i)^2}{\sqrt{\sum_{i=1}^n \bar{x}_i^2} \cdot \sqrt{\sum_{i=1}^n \bar{y}_i^2}} \cdot 100\% \quad (18)$$

In these two expressions, x_i is measured, y_i denotes the simulated self-excited forces, and \bar{x}_i and \bar{y}_i are the peaks of the time series. The correlation coefficients and peak errors for all the tests conducted are listed in Table 5, and Fig. 14 shows exemplary time series of the measured and predicted self-excited forces at the mid-span (Pos. 3).

The results show that the measured and predicted self-excited lift forces and pitching moment correspond in an excellent manner. This indicates that Scanlan's model for the self-excited forces provides very good results for the lift force and the pitching moment along the entire span. This implies that the varying phase lags and the amplitudes of the horizontal and torsional motions along the span do not affect the accuracy of the predicted self-excited forces. It is also interesting to see that despite the fact that the load model has been derived while assuming small vibration amplitudes, it still holds at relatively large amplitudes.

Table 5 Correlation coefficient and peak error between measured and predicted aeroelastic forces induced during flutter

Position	Frequency scale	Air velocity [m/s]	Drag		Lift		Pitch	
			ρ_{xy}	$P_{err}[\%]$	ρ_{xy}	$P_{err}[\%]$	ρ_{xy}	$P_{err}[\%]$
Pos. 1	4	6.59	0.465	256.9	0.999	0.244	1.00	0.033
Pos. 1	6	9.89	0.537	255.5	0.995	1.089	0.999	0.071
Pos. 1	7	11.53	0.658	202.8	0.998	0.867	0.999	0.049
Pos. 2	4	6.59	0.427	231.8	0.996	0.670	1.00	0.039
Pos. 2	6	9.89	0.541	191.2	0.998	0.530	1.00	0.074
Pos. 2	7	11.53	0.570	193.1	0.997	1.156	0.999	0.071
Pos. 3	4	6.59	0.500	127.7	0.998	0.335	0.999	0.057
Pos. 3	6	9.89	0.560	130.7	0.996	0.842	0.999	0.088
Pos. 3	7	11.53	0.633	136.3	0.995	1.348	0.999	0.106
Average			0.543	191.8	0.997	0.787	0.999	0.065


 Fig. 14 Measured vs predicted forces induced during the flutter motion at the bridge mid-span; $V = 6.59$ m/s

On the other hand, the prediction of the self-excited drag force is inaccurate. Analysis of the time series revealed that there is an additional higher-order harmonic contribution at $2\omega_{CR}$ in the recorded drag force. The applied motion was purely sinusoidal; thus, the input motion cannot explain the higher-order self-excited forces. Some higher order contributions were also observed in the standard forced vibration tests. The self-excited drag is very challenging to measure since it is very small for small amplitude motion. It is therefore much harder to distinguish the higher order contributions from inaccuracies introduced by inaccurate cancellation of inertia forces and other uncertainties. Second-order effects have, however, been observed before (Wu and Kareem 2013). Chen *et al.* (2005) reported the presence of higher-order harmonics in self-excited lift and pitch under nearly purely torsional oscillations. They observed significant contributions from second- and third-order harmonics for a bluff cross-section, while a test of a thin plate did not provide any significant higher-order effects. More recent numerical studies by Xu *et al.* (2016) focused on the higher-order self-excited drag force. They reported that the second-order drag force can be dominant

for a streamlined section when it undergoes torsional oscillations. The results presented herein confirm the findings of these numerical studies and should be considered for further study. There exist nonlinear models for self-excited forces. Studies have shown that Volterra series (Wu and Kareem 2014), artificial neural networks (Wu and Kareem 2013) and rheological models (Diana *et al.* 2008) (Diana *et al.* 2010) are possible alternatives. Detailed modelling of nonlinear self-excited forces is considered out of the scope of this paper, but it is interesting to consider a simple expression, which should give a reasonable approximation for single harmonic motion. The following expression, which includes two harmonic components, has therefore been fitted to the measured self-excited forces to assess the importance of the second-order effects

$$q_{se,n}(t) = A_n \sin(\omega_{CR}t + \varphi_{A_n}) + B_n \sin(2\omega_{CR}t + \varphi_{B_n}) \quad (19)$$

Table 6 shows the amplitude ratios B/A for all the performed tests; Table 7 compares the accuracy of the predicted drag force when considering only the first-order and both the first- and second-order effects.

Table 6 The ratio between the amplitudes of second- and first-order harmonics in the measured self-excited forces

Position	Frequency scale	Air velocity [m/s]	Effects of the second-order harmonics [%]		
			Drag	Lift	Pitch
Pos. 1	4	6.59	132.54	3.53	1.39
Pos. 1	6	9.89	114.63	4.98	1.48
Pos. 1	7	11.53	94.32	4.27	1.38
Pos. 2	4	6.59	189.95	4.87	1.75
Pos. 2	6	9.89	151.15	5.39	2.12
Pos. 2	7	11.53	135.06	5.23	1.98
Pos. 3	4	6.59	157.50	5.16	1.65
Pos. 3	6	9.89	132.70	5.83	1.97
Pos. 3	7	11.53	106.28	5.74	1.95
Average			134.9	5.00	1.74

Table 7 Accuracy of the predicted self-excited drag force considering only first-order and both first- and second-order effects

Position	Frequency scale	Air velocity [m/s]	First-order harmonic		First- + Second-order harmonics	
			ρ_{xy}	$P_{err} [\%]$	ρ_{xy}	$P_{err} [\%]$
Pos. 1	4	6.59	0.535	107.6	0.897	13.4
Pos. 1	6	9.89	0.575	94.0	0.877	16.1
Pos. 1	7	11.53	0.680	67.4	0.933	8.6
Pos. 2	4	6.59	0.429	167.1	0.922	9.6
Pos. 2	6	9.89	0.542	99.2	0.982	1.9
Pos. 2	7	11.53	0.570	91.1	0.958	5.4
Pos. 3	4	6.59	0.523	129.6	0.974	3.2
Pos. 3	6	9.89	0.565	101.4	0.936	8.5
Pos. 3	7	11.53	0.638	78.7	0.929	10.0
Average			0.562	104.0	0.934	8.5

As expected, the second-order effects strongly influence the self-excited drag force. In fact, for 8 out of the 9 tests, the magnitude of the second-order harmonic was larger than that of the first one. Table 7 also shows that the predicted drag force is greatly improved when including the second-order effects. For the lift and pitching moment, the measured second-order contributions were much smaller. These observations are clearly strongly dependent on the aerodynamic characteristics of the particular section considered. The self-excited forces for sections that have almost linear force coefficients in the considered range of effective angles of attack will in general give an output that is linear even for large angles of attack.

3.5 Amplitude dependency

The results in the previous chapter show that the self-excited lift force and pitching moment are predicted very accurately for the motion considered, while the predicted drag force is inaccurate due to strong second-order contributions. Previous studies have shown that the aerodynamic derivatives might be amplitude dependent even when relatively small amplitudes are considered (Chen *et al.* 2005). It is therefore of interest to study how the model of the self-excited force performs when considering increasing amplitudes, which will be the case when the mean wind velocity is slightly higher than the critical velocity. The diverging flutter motion has been obtained

with Eq. (10), assuming a negative damping ratio of $\zeta = -0.15\%$.

Two of the previously considered frequency scales $S_f = 4$ and $S_f = 6$ and all three positions in Fig. 7 have been considered in this study. Fig. 15 shows simulated time histories of the flutter motion at the mid-span of the bridge considering a mean wind velocity of 9.9 m/s and a critical frequency of 1.67 Hz. The maximum horizontal displacement is approximately 1% of the width of the bridge deck, while the maximum vertical displacement is approximately 60% of the height of the girder. The amplitudes of the torsional vibrations range from 2° to 13° .

The load model presented in Eq. (12) is, strictly speaking, only valid for harmonic oscillations of the bridge deck, which is not the case when negative damping is introduced. Fig. 16 shows the FFT of the motion history. The motion is very narrow banded, which implies that assuming a single harmonic motion and using the values of the aerodynamic derivatives presented in Table 4 yield a fair approximation.

Fig. 17 presents a comparison of the predicted and measured self-excited forces induced during the wind tunnel test corresponding to the motion history displayed in Fig. 15.

A near-perfect match between the predicted and measured lift and pitching moment values can be observed, while the drag predictions seem to have been more accurate at the beginning of the test.

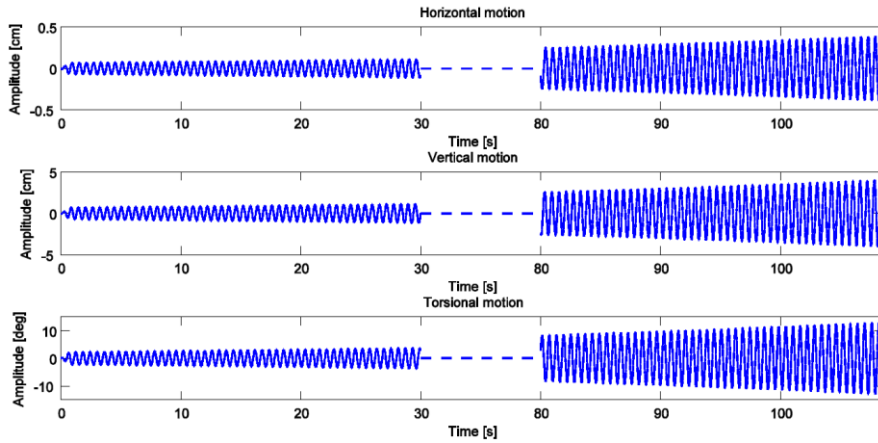


Fig. 15 Time series of the flutter motion at the mid-span of the bridge when assuming negative damping

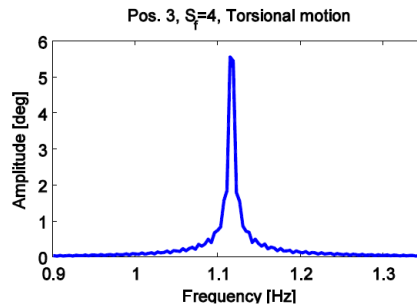


Fig. 16 FFT of the torsional motion in Fig. 15

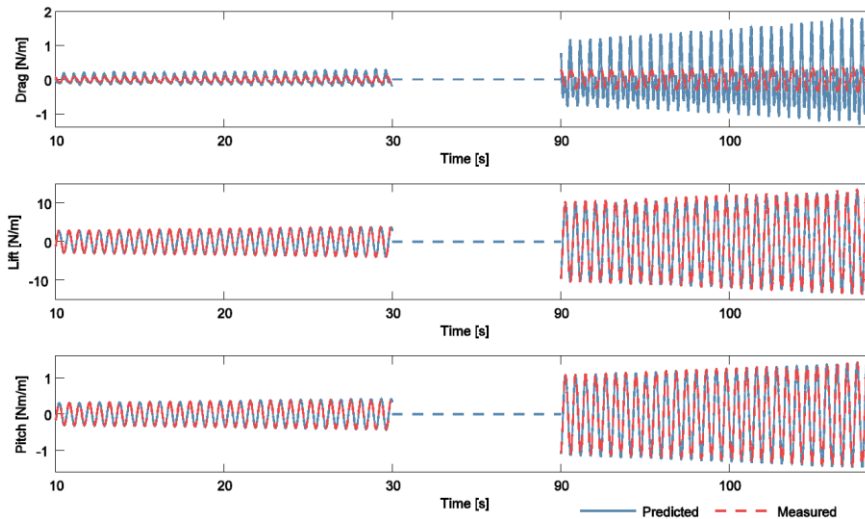


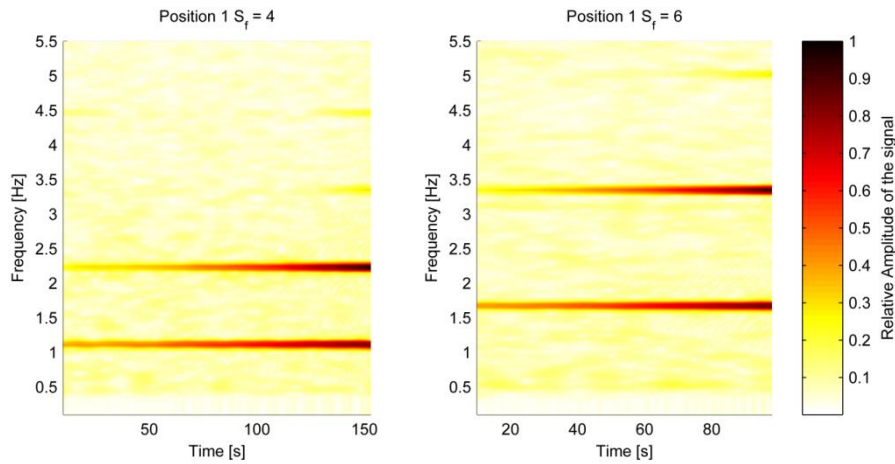
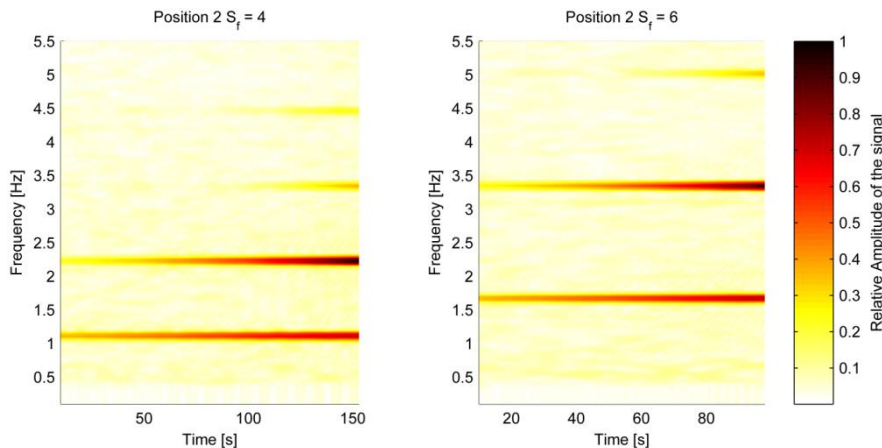
Fig. 17 Measured vs predicted self-excited forces induced during motion at position 3 for $S_f=4$

As the amplitude of the vibrations increases, the higher-order harmonic contributions start to play a crucial role in the measured self-excited drag. The recorder time series were divided into five equal time intervals to study the changes in the coefficient of determination - R^2 between predicted and measured forces. Results presented in Table 8 confirm that the accuracy of drag force predictions drops when vibrations increase, while in case of lift and pitch this

effect is negligible. Spectrograms in Fig. 18 show how the frequency content of the recorded self-excited drag changes, when flutter motion strengthens. Values on the spectrograms have been scaled to show relative amplitude of the harmonic signals, where 1 indicated largest recorder amplitude of a single harmonic for the entire time of experiment.

Table 8 Coefficient of determination of the measured versus predicted self-excited forces considering segments of the motion

Part of the total time series	R^2 – coefficient of determination								
	Drag			Lift			Pitch		
	Pos. 1	Pos. 2	Pos. 3	Pos. 1	Pos. 2	Pos. 3	Pos. 1	Pos. 2	Pos. 3
0.0-0.2	0.323	0.483	0.645	0.997	0.998	0.997	0.999	0.999	0.999
0.2-0.4	0.345	0.432	0.587	0.998	0.998	0.998	0.999	0.999	0.999
0.4-0.6	0.300	0.359	0.485	0.998	0.997	0.997	0.999	0.999	0.999
0.6-0.8	0.237	0.261	0.364	0.997	0.996	0.995	0.999	0.999	0.999
0.8-1.0	0.164	0.161	0.230	0.995	0.994	0.995	0.999	0.994	0.995

Fig. 18 Spectrograms of the measured drag force under flutter motion corresponding to $0.25L$ (pos. 1)Fig. 19 Spectrograms of the measured drag force under flutter motion corresponding to $0.4L$ (pos. 2)

As expected, Fig. 18 clearly confirms the presence of the higher-order harmonics in the measured self-excited drag force. For all of the tested locations and frequency scales used, the following conclusions can be drawn. The first-order harmonic prevails at the early part of the time series, where amplitudes of the motion are relatively small. As the vibrations increase, higher-order harmonic contributions start to appear. The second-order harmonic

especially requires special attention, as it increases faster than the first-order harmonic. The second-order component dominates in the last part of the time series for all the cases considered. Fig. 21 shows spectrograms of the lift force and the pitching moment. Higher-order effects are also clearly present in the last part of the time series but of much less relative magnitude than for the self-excited drag force.

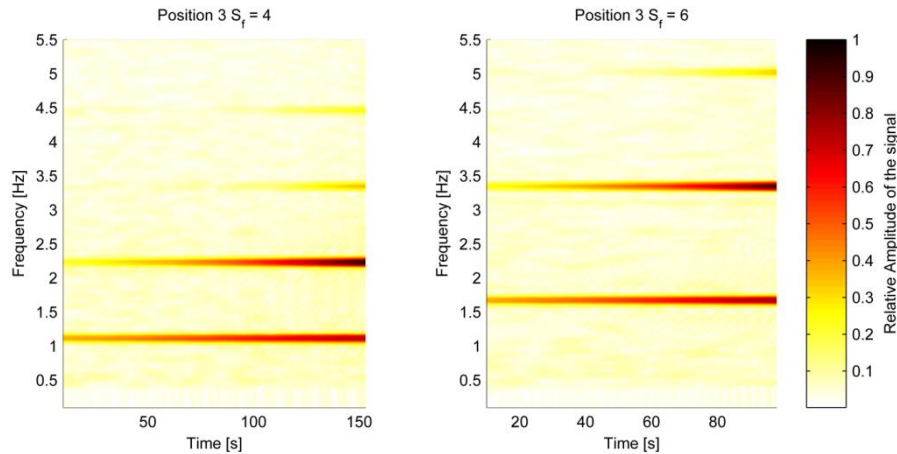


Fig. 20 Spectrograms of the measured drag force under flutter motion corresponding to $0.5L$ (pos. 3)

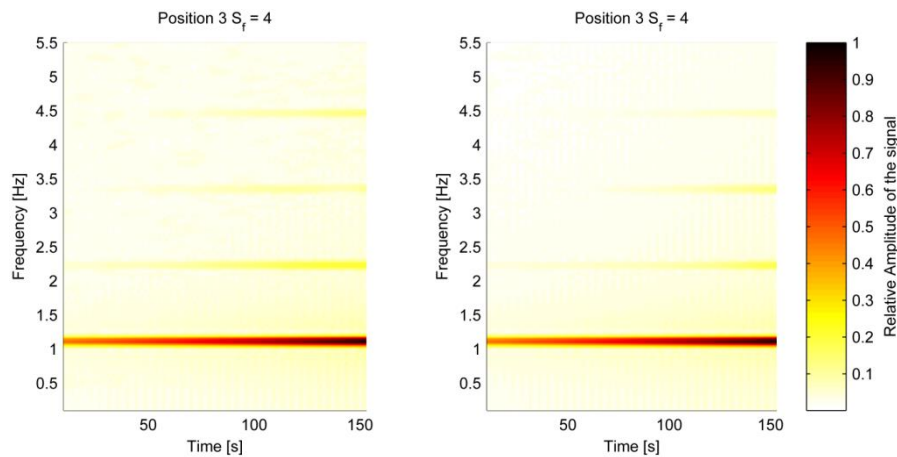


Fig. 21 Spectrograms of the measured lift force (left) and pitching moment (right) for the scaled flutter motion corresponding to $0.5L$ (pos. 3)

4. Conclusions

The modeling of self-excited forces is of crucial importance when assessing the flutter stability limit of long-span, cable-supported bridges. This is particularly evident when several still-air vibration modes participate in the flutter motion, making the ratio of the amplitudes and the phase lag between the horizontal, vertical and torsional motions vary along the span of the structure. Forced vibration technique with a use of section model has been used to investigate the accuracy of the self-excited forces predicted during flutter motion using aerodynamic derivatives. The full set of 18 aerodynamic derivatives of the cross-section of the Hardanger Bridge was first identified using a standard forced vibration procedure. Predicted and measured self-excited forces for the flutter motion were compared to assess how well the aerodynamic derivatives capture the self-excited forces along the span. The flutter mode of the bridge was obtained using the multimode approach, and since the flutter mode is complex and differs along the bridge span, flutter motions at the mid-span, at the quarter-span and in close proximity to the mid-

span of the bridge were considered in this study. Several mean wind velocity and motion frequency combinations that correspond to the critical reduced velocity at full scale were considered to study if they affect the accuracy of the predicted forces.

The experimental results show that the aerodynamic derivatives identified using a standard forced vibration test capture the self-excited lift force and pitching moment very well since the predictions correspond to the measurements in an excellent manner for all tested position as well as all mean wind velocity and frequency combinations. The predicted self-excited drag force does not, however, correspond well to the measured self-excited drag force. The recorded time series revealed a very strong influence from second-order effects that dominates the drag force. The second-order effects are also visible for the lift and pitching moment, but they are very small compared with the first-order effects. It was also shown that by including the second-order contribution in the model of the self-excited forces, the predictions of the drag force can be significantly improved. The effects of the amplitude on the accuracy of the prediction of the self-excited forces during flutter

motion were investigated by considering a divergent time series that corresponds to negative damping. For small amplitudes, the self-excited drag force is nearly linear, while higher-order harmonics appear when the amplitudes become larger. The measured self-excited lift and pitching moment values correspond in an excellent manner, even for the largest amplitudes considered, although less influential higher-order contributions were also noticed for these force components.

Acknowledgments

This research was conducted with financial support from the Norwegian Public Roads Administration. The authors gratefully acknowledge this support.

References

- Adaramola, M.S. and Krogstad, P.Å. (2009), "Model tests of a horizontal axis wind turbine in yawed condition. In European offshore wind conference and exhibition", *Proceedings of the European Offshore Wind Conference and Exhibition*, Stockholm.
- Agar, T.J.A. (1989), "Aerodynamic flutter analysis of suspension bridges by a modal technique", *Eng. Struct.*, **11**(2), 75-82.
- Andersen, M.S., Johansson, J., Brandt, A. and Hansen, S.O. (2016), "Aerodynamic stability of long span suspension bridges with low torsional natural frequencies", *Eng. Struct.*, **120**, 82-91.
- Bartoli, G. and Mannini, C. (2008), "A simplified approach to bridge deck flutter", *J. Wind Eng. Ind. Aerod.*, **96**(2), 229-256.
- Cao, B. and Sarkar, P.P. (2012), "Identification of Rational Functions using two-degree-of-freedom model by forced vibration method", *Eng. Struct.*, **43**, 21-30.
- Caracoglia, L. and Jones, N.P. (2003), "Time domain vs. frequency domain characterization of aeroelastic forces for bridge deck sections", *J. Wind Eng. Ind. Aerod.*, **91**, 371-402.
- Chen, X. (2007), "Improved understanding of bimodal coupled bridge flutter based on closed-form solutions", *J. Struct. Eng.*, **133**(1), 22-31.
- Chen, X., Kareem, A. and Matsumoto, M. (2001), "Multimode coupled flutter and buffeting analysis of long span bridges", *J. Wind Eng. Ind. Aerod.*, **89**(7-8), 649-664.
- Chen, Z.Q., Yu, X. D., Yang, G. and Spencer, B.F. (2005), "Wind-induced self-excited loads on bridges", *J. Struct. Eng.*, **131**, 1783-1793.
- Costa, C. (2007), "Aerodynamic admittance functions and buffeting forces for bridges via indicial functions", *J. Fluid. Struct.*, **23**(3), 413-428.
- Diana, G., Resta, F., and Rocchi, D. (2008). "A new numerical approach to reproduce bridge aerodynamic non-linearities in time domain." *Journal of Wind Engineering and Industrial Aerodynamics*, **96**, 1871-1884.
- Diana, G., Resta, F., Zasso, A., Belloli, M. and Rocchi, D. (2004), "Forced motion and free motion aeroelastic tests on a new concept dynamometric section model of the Messina suspension bridge", *J. Wind Eng. Ind. Aerod.*, **92**, 441-462.
- Diana, G., Rocchi, D. and Belloli, M. (2015), "Wind tunnel : a fundamental tool for long-span bridge design", *Structure and Infrastructure Engineering: Maintenance, Management, Life-Cycle Design and Performance*, **11**(4), 533-555.
- Dunham, K.K. (2016), "Coastal Highway Route E39 – Extreme Crossings", *Transportation Research Procedia*, **14**(2352), 494-498.
- Fenerci, A. and Ø iseth, O. (2015), "Full-scale measurements on the Hardanger Bridge during strong winds", *In Dynamics of Civil Structures, Volume 2, Conference Proceedings of the Society for Experimental Mechanics Series*, 237-245.
- Fenerci, A. and Ø iseth, O. (2017), "Measured buffeting response of a long-span suspension bridge compared with numerical predictions based on design wind spectra", *J. Struct. Eng.*, **147**, 1-15.
- Fenerci, A., Ø iseth, O. and Rönnquist, A. (2017), "Long-term monitoring of wind field characteristics and dynamic response of a long-span suspension bridge in complex terrain", *Eng. Struct.*, **143**, 269-284.
- Fuller, R.G., Lang, C.R. and Lang, R.H. (2000), *Twin views of the Tacoma Narrows Bridge collapse*, American Association of Physics Teachers.
- Ge, Y.J. and Tanaka, H. (2000), "Aerodynamic flutter analysis of cable-supported bridges by multi-mode and full-mode approaches", *J. Wind Eng. Ind. Aerod.*, **86**(2-3), 123-153.
- Gu, M., Zhang, R. and Xiang, H. (2000), "Identification of flutter derivatives of bridge decks", *J. Wind Eng. Ind. Aerod.*, **84**, 151-162.
- Han, Y. Liu, S., Hu, J.X., Cai, C.S., Zhang, J. and Chen, Z. (2014), "Experimental study on aerodynamic derivatives of a bridge cross-section under different traffic flows", *J. Wind Eng. Ind. Aerod.*, **133**, 250-262.
- Hansen, O.S. et al. (2009), "The Hardanger Bridge static and dynamic wind tunnel tests with a section model", *Prepared for: Norwegian Public Roads Administration Revision 2*.
- Hua, X.G. and Chen Z.Q. (2008), "Full-order and multimode flutter analysis using ANSYS", *Finite Elem. Anal. Des.*, **44**, 537-551.
- Huang, L., Liao, H., Wang, B. and Li, Y. (2009), "Numerical simulation for aerodynamic derivatives of bridge deck", *Simul. Model. Pract. Th.*, **17**(4), 719-729.
- Iwamoto, M. and Fujino, Y. (1995), "Identification of flutter derivatives of bridge deck from free vibration data", *J. Wind Eng. Ind. Aerod.*, **55**, 55-63.
- Jain, A., Jones, N.P. and Scanlan, R.H., (1996). "Coupled flutter and buffeting analysis of long-span bridges", *J. Struct. Eng.*, **122**(7), 716-725.
- Jones, N.P. Scanlan, R.H., Sarkar, P.P. and Singha, L. (1995), "The effect of section model details on aeroelastic parameters", *J. Wind Eng. Ind. Aerod.*, **54-55**, 45-53.
- Katsuchi, B.H., Jones, N.P. and Scanlan, R.H. (1999), "Multimode coupled flutter and buffeting analysis of the Akashi-Kaikyo Bridge", *J. Struct. Eng.*, **125**(1), 60-70.
- Katsuchi, H. Jones, N.P., Scanlan, R.H. and Akiyama, H. (1998), "Multi-mode flutter and buffeting analysis of the Akashi-Kaikyo bridge", *J. Wind Eng. Ind. Aerod.*, **77-78**, 431-441.
- Kvåle, K.A., Sigbjörnsson, R. and Ø iseth, O. (2016), "Modelling the stochastic dynamic behaviour of a pontoon bridge: A case study", *Comput. Struct.*, **165**, 123-135.
- Körlin, R. and Starossek, U. (2007), "Wind tunnel test of an active mass damper for bridge decks", *J. Wind Eng. Ind. Aerod.*, **95**(4), 267-277.
- Manzoor, S., Hémon, P. and Amandolese, X., (2011), "On the aeroelastic transient behaviour of a streamlined bridge deck section in a wind tunnel", *J. Fluid. Struct.*, **27**, 1216-1227.
- Matsumoto, M. (1996), "Aerodynamic damping of prisms." *J. Wind Eng. Ind. Aerod.*, **59**, 159-175.
- Matsumoto, M., Mizuno, K., Okubo, K., Ito, Y. and Matsumiya, H. (2007). "Flutter instability and recent development in stabilization of structures", *J. Wind Eng. Ind. Aerod.*, **95**(9-11), 888-907.
- Matsumoto, M., Matsumiya, H., Fujiwara, S. and Ito, Y. (2008), "New Consideration on Flutter Properties basing on SBS - Fundamental Flutter Mode, Similar Selberg's Formula,

- Torsional Divergence Instability, and New Coupled Flutter Phenomena affected by Structural Coupling”, In *BBA VI Internarional Colloquium*, Milano.
- Mishra, S.S., Kumar, K. and Krishna, P. (2008), “Multimode flutter of long-span cable-stayed bridge based on 18 experimental aeroelastic derivatives”, *J. Wind Eng. Ind. Aerod.*, **96**(1), 83-102.
- Miyata, T., Tada, K., Sato, H., Katsuchi, H. and Hikami, Y. (1994), “New findings of coupled-flutter in full model wind tunnel tests on the Akashi Kaikyo Bridge”, *Proceedings of the Symposium on Cable-Stayed and Suspension Bridges, Association Francaise Pour la Construction*, Deauville.
- Nakamura, Y. (1978), “An analysis of binary flutter of bridge deck section”, *J. Sound Vib.*, **57**, 471-482.
- Namini, A., Albrecht, P. and Bosch, H. (1992), “Finite element-based flutter analysis of cable-suspended bridges”, *J. Struct. Eng.*, **118**(6), 1509-1526.
- NI CompactRIO (2017), National Instruments, <<http://www.ni.com/compactrio/>>(Mai 07, 2017).
- Ø iseth, O. and Sigbjörnsson, R. (2011), “An alternative analytical approach to prediction of flutter stability limits of cable supported bridges”, *J. Sound Vib.*, **330**(12), 2784-2800.
- Ø iseth, O., Rönquist, A. and Sigbjörnsson, R. (2010), “Simplified prediction of wind-induced response and stability limit of slender long-span suspension bridges, based on modified quasi-steady theory: A case study”, *J. Wind Eng. Ind. Aerod.*, **98**(12), 730-741.
- Ø iseth, O., Rönquist, A. and Sigbjörnsson, R. (2011), “Time domain modeling of self-excited aerodynamic forces for cable-supported bridges: A comparative study”, *Comput. Struct.*, **89**(13-14), 1306-1322.
- Ø iseth, O., Rönquist, A. and Sigbjörnsson, R. (2012), “Finite element formulation of the self-excited forces for time-domain assessment of wind-induced dynamic response and flutter stability limit of cable-supported bridges”, *Finite Elem. Anal. Des.*, **50**, 173-183.
- Qin, X.R., Kwok, K.C.S., Fok, C.H. and Hitchcock, P.A. (2009). “Effects of frequency ratio on bridge aerodynamics determined by free-decay sectional model tests”, *Wind Struct.*, **12**(5), 413-424.
- Salvatori, L. and Borri, C. (2007), “Frequency- and time-domain methods for the numerical modeling of full-bridge aeroelasticity”, *Comput. Struct.*, **85**(11-14), 675-687.
- Sarkar, P.P., Caracoglia, L., Haan, F.L., Sato, H. and Murakoshi, J. (2009), “Comparative and sensitivity study of flutter derivatives of selected bridge deck sections, Part 1: Analysis of inter-laboratory experimental data”, *Eng. Struct.*, **31**(1), 158-169.
- Sarkar, P.P., Chowdhury, A.G. and Gardner, T.B. (2004), “A novel elastic suspension system for wind tunnel section model studies”, *J. Wind Eng. Ind. Aerod.*, **92**, 23-40.
- Sarwar, M.W., Ishihara, T., Shimada, K., Yamasaki, Y. and Ikeda, T. (2008), “Prediction of aerodynamic characteristics of a box girder bridge section using the LES turbulence model”, *J. Wind Eng. Ind. Aerod.*, **96**(10-11), 1895-1911.
- Scanlan, B.R.H. and Jones, N.P. (1990), “Aeroelastic analysis of cable-stayed bridges”, *J. Struct. Eng.*, **116**(2), 279-297.
- Scanlan, R.H. (1997), “Amplitude and turbulence effects on bridge flutter derivatives”, *J. Struct. Eng.*, **123**(2), 232-236.
- Scanlan, R.H. and Tomko, J. (1971), “Airfoil and bridge deck flutter derivatives”, *J. Eng. Mech. Div.*, **97**(6), 1717-1733.
- Selberg, A. (1961), “Oscillation and Aerodynamic Stability of Suspension Bridges”, *Acta polytechnica Scandinavica Civil Engineerin and Building Construction Series*.
- Siedziako, B., Ø iseth, O. and Rönquist, A. (2016a), “A new setup for section model tests of bridge decks”, *Proceedings of the 12th UK Conference on Wind Engineering*, Nottingham.
- Siedziako, B., Ø iseth, O. and Rönquist, A. (2016b), “Identification of aerodynamic properties of bridge decks in arbitrary motion”, In *Special Topics in Structural Dynamics, Volume 6: Proceedings of the 34th IMAC, A Conference and Exposition on Structural Dynamics*.
- Siedziako, B., Ø iseth, O. and Rönquist, A. (2017), “An enhanced forced vibration rig for wind tunnel testing of bridge deck section models in arbitrary motion”, *J. Wind Eng. Ind. Aerod.*, **164**, 152-163.
- Simiu, E. and Scanlan, R.H. (1996), *Wind Effects on Structures* 3rd Ed., Wiley, New York, NY, USA.
- Singh, L., Jones, N.P., Scanlan, R.H. and Lorendeaux, O. (1996), Identification of lateral flutter derivatives of bridge decks”, *J. Wind Eng. Ind. Aerod.*, **60**(1-3), 81-89.
- Takizawa, K., Bazilevs, Y., Tezduyar, T.E., Hsu, M.C., Ø iseth, O., Mathisen, K.M., Kostov, N. and McIntyre, S. (2014), “Engineering analysis and design with ALE-VMS and space-time methods”, *Arch. Comput. Method. E.*, **21**(481), 481-508.
- Ukeguchi, N., Sakata, H. and Nishitani, H. (1966), “An investigation of aerolastic initality of suspension bridges”, In *Symposium on Suspension Bridges*, Lisbon.
- Wu, T. and Kareem, A. (2014), “Simulation of nonlinear bridge aerodynamics: A sparse third-order Volterra model”, *J. Sound Vib.*, **333**(1), 178-188.
- Xu, F.Y., Wu, T., Ying, X.Y. and Kareem, A. (2016), “Higher-order self-excited drag forces on bridge decks”, *Technical Note in J. Eng. Mech.*, **142**(3).
- Xu, Y. Ø iseth, O., Naess, A. and Moan, T. (2017), “Prediction of long-term extreme wind-induced load effects for cable-supported bridges using time-domain simulations”, *Eng. Struct.*, **148**, 239-253.
- Zhang, X. and Brownjohn, J.M.W. (2005), “Some considerations on the effects of the P-derivatives on bridge deck flutter”, *J. Sound Vib.*, **283**(3-5), 957-969.
- Zhu, Z.W., Gu, M. and Chen, Z.Q. (2007), “Wind tunnel and CFD study on identification of flutter derivatives of a long-span self-anchored suspension bridge”, *Comput.-Aided Civil Infrastruct. Eng.*, **22**(8), 541-554.

CC